Title

ADCP Bias and Stokes Drift in AUV-Based Velocity Measurements

Journal

Journal of Atmospheric and Oceanic Technology, 34(9)

ISSN

0739-0572

Authors

Amador, André
Jaramillo, Sergio
Pawlak, Geno

Publication Date

2017

DOI

10.1175/jtech-d-16-0182.1

Peer reviewed

ADCP Bias and Stokes Drift in AUV-Based Velocity Measurements

ANDRÉ AMADOR

Mechanical and Aerospace Engineering, University of California, San Diego, La Jolla, California

SERGIO JARAMILLO

Shell Global Solutions, Houston, Texas

GENO PAWLAK

Mechanical and Aerospace Engineering, University of California, San Diego, La Jolla, California

(Manuscript received 21 September 2016, in final form 3 July 2017)

ABSTRACT

A theoretical model is developed to describe how autonomous underwater vehicle (AUV)-based current measurements are influenced by a surface wave field. The model quantifies a quasi-Lagrangian, wave-induced velocity bias as a function of the local wave conditions, and the vehicle's depth and velocity using a first-order expansion of the linear wave solution. The theoretical bias is verified via field experiments carried out off the coast of Oahu, Hawaii. Spatially averaged along- and cross-track AUV velocity measurements are calculated over one effective wavelength and compared with time-averaged, fixed ADCP measurements in a range of wave and current conditions. The wave-induced bias is calculated using wave directional spectra derived from fixed ADCP data. Ensemble-averaged velocity differences ($\langle \Delta V \rangle = \langle V_{\mathrm{AUV}} - V_{\mathrm{ADCP}} \rangle$) confirm the presence of the wave-induced bias $O(1\text{–}5)$ cm s^{-1} and reveal an additional bias in the direction of the vehicle motion $O(1)$ cm s^{-1}. The analysis considers velocity measurements made using a Remote Environmental Monitoring Units (REMUS) 100 AUV, but the content applies to any small AUV (vehicle size $\ll$ wavelength) immersed in a wave field.

1. Introduction

The advent of small, manually deployable autonomous underwater vehicles (AUVs) equipped with Doppler velocity logs (DVLs) has revolutionized the way in which we monitor marine environments. The portability and economy offered by AUVs provides the opportunity for extensive hydrodynamic mapping in a variety of environments, some of which were previously unattainable by traditional ship-based techniques. For example, AUVs have been used for high-resolution hydrographic surveys in deep water (Stansfield et al. 2001, 2003) and submarine canyons (Sumner et al. 2013), for turbulence microstructure observations in the continental shelf (Goodman and Wang 2009), to observe plume dispersion in coastal waters (Rogowski et al. 2014) and over coral reefs (Jones et al. 2008), and to measure velocity profiles in shallow lakes and riverine environments (Brown et al. 2011). In each of these cases, AUVs have provided an efficient solution for collecting spatial data, including flow velocities.

This dramatic increase in the amount of AUV-based data has motivated the need for effective measurement practices and the assessment of error sources that affect the reliability of the measurements. Of particular concern are systematic errors in the velocity measurements, which cannot be eliminated or reduced via averaging and can complicate the measurement of the flow field. In coastal flows, for example, systematic errors of several centimeters per second can become important because coastal currents can be comparable in magnitude, especially in the cross-shore direction.

AUV subsurface navigation is typically achieved using onboard dead-reckoning systems based on DVLs and a combination of inertial sensors (accelerometers and/or gyroscopes) and a magnetic compass. DVLs use acoustic measurements to determine the vehicle's velocity relative to the seabed. Dead-reckoning navigation is aided by long baseline (LBL) acoustic positioning, which triangulates the position of the vehicle

Corresponding author: André Amador, a1amador@ucsd.edu

DOI: 10.1175/JTECH-D-16-0182.1

using acoustic signals from widely spaced fixed acoustic transponders (Paull et al. 2014). The navigation algorithm then integrates the measurements from the navigation sensors to give high-rate estimates of the position, orientation, and velocity of the vehicle.

DVLs determine a vehicle's velocity vector using multiple (typically three or four) downward acoustic beams oriented at angles relative to each other, commonly in a convex arrangement. The Doppler shift in the bottom reflection from each beam is processed to determine the velocity component in the beam direction. With four angled beams, the three-dimensional velocity vector for the vehicle can be calculated along with an error estimate. DVLs can also be configured as acoustic Doppler current profilers (ADCP) to measure water velocities. In this case, Doppler shifts are calculated from water column reflections within discrete range intervals (bins) along each beam. Velocity components along each beam are then combined to obtain a profile of the three-dimensional water velocity vector. Since the beams diverge with distance from the DVL (or ADCP), the effective sampling volume similarly increases.

To construct velocity profiles in an Earth-based reference frame from a moving platform, the velocity of the instrument relative to the bottom must be removed from the raw water column velocity estimate. Fong and Monismith (2004) examined the accuracy of a DVL bottom-tracking system using concurrent high-resolution kinematic GPS data and found that average vessel speeds were in excellent agreement over multiple transects of several hundred meters in length. Because of the inherent error in individual ADCP velocity samples, AUV-based measurements often rely on spatial averaging to deduce useful estimates of water current velocities (Fong and Jones 2006).

In this paper we focus on two unrelated types of bias errors that affect AUV-based velocity estimates. First, we examine a wave-induced bias that is closely related to Stokes drift. Second, consistent with a previously observed phenomenon (Fong and Monismith 2004; Fong and Jones 2006), we report on the presence of an additional bias in the direction of the vehicle motion. This work considers velocity measurements made using a Remote Environmental Monitoring Units (REMUS) 100 AUV (Hydroid Inc.) outfitted with a four-beam 1200-kHz RD Instruments DVL (similar to the RD Instruments Workhorse ADCP). The REMUS 100 is a compact (160 cm in length, 19 cm in diameter), lightweight (37 kg), torpedo-shaped AUV designed for operation in coastal environments (Brown et al. 2004; Moline et al. 2005; Amador et al. 2015). The analysis here, however, applies to any small AUV (vehicle size $\ll$ wavelength) immersed in a wave field.

In section 2 we show how AUV-based current measurements may be influenced by perturbations in the vehicle trajectory caused by the wave field. We develop a theoretical framework to quantify a wave-induced velocity bias as a function of the local wave conditions, and the vehicle's depth and velocity. In section 3 we describe our field observations and present an analysis of a series of tests in wave-forced, fringing coral reef environments to examine the effects of spatial averaging in AUV-based velocity measurements. We compare the expected uncertainty estimates to root-mean-square deviations (RMSD) of depth-averaged, normalized velocity differences, to show that wave-induced uncertainties dominate the random error present in our data. In section 4 we calculate ensemble-averaged along- and cross-track velocity differences ($\langle \Delta V \rangle = \langle V_{\mathrm{AUV}} - V_{\mathrm{ADCP}} \rangle$) from fixed ADCP measurements to investigate the accuracy of AUV-based water velocity measurements and to explore the presence of velocity biases. Results are discussed and summarized in sections 5 and 6, respectively.

2. Background

Although the REMUS 100 can be programmed to maintain a prescribed depth and speed, surface waves have the potential to influence its dynamics. In practice, the wave field will perturb the vehicle's speed and vertical displacement to a degree, especially in shallow water, in routes near the sea surface and in the presence of large waves (e.g., Goodman et al. 2010; Sgarioto 2011; Amador et al. 2015; Haven and Terray 2015). Here we show how the influence of the wave velocity field on the vehicle trajectory can lead to a bias in spatially averaged velocity measurements, and we develop a theoretical framework to quantify this bias.

a. Vehicle trajectory

Consider an AUV traversing a monochromatic wave field, operating at some constant average depth Z_0, as shown in Fig. 1. Let a represent the wave amplitude, h is the local depth, σ is the wave radian frequency, k is the wavenumber, and $c = \sigma/k$ is the phase speed. We assume inviscid, irrotational flow and that the vehicle closely follows the horizontal and vertical water displacements produced by surface gravity waves. Hence, the velocity of the vehicle is given by

$$u_{\mathrm{AUV}}(x,z,t) = U + u_w \quad \text{and} \tag{1}$$

$$w_{\mathrm{AUV}}(x,z,t) = w_w, \tag{2}$$

where U is the constant horizontal cruising speed of the vehicle (relative to the water); and

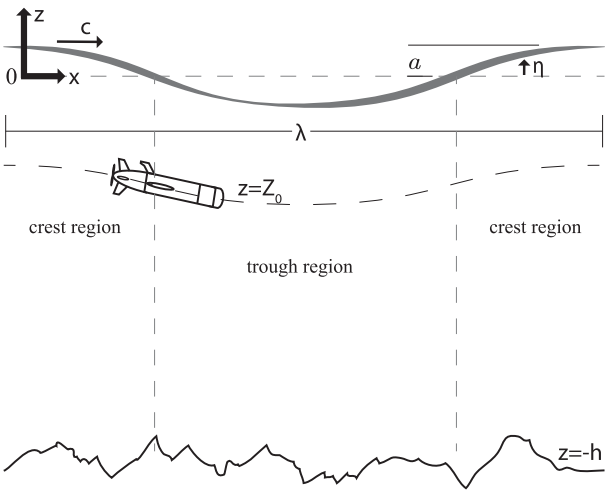

FIG. 1. AUV traversing a monochromatic wave field. Note the coordinate system ($z = 0$ at the mean sea surface $\overline{\eta}$), the crest ($\eta > 0$) and trough ($\eta < 0$) regions of the wave, and key parameters: wave amplitude (a), wavelength (λ), wave speed (c), water depth (h), and vehicle depth (Z_0).

$$u_w = a\sigma \frac{\cosh[k(z+h)]}{\sinh(kh)} \cos(kx - \sigma t) \quad \text{and} \tag{3}$$

$$w_w = a\sigma \frac{\sinh[k(z+h)]}{\sinh(kh)} \sin(kx - \sigma t) \tag{4}$$

are the components of wave orbital velocity from linear theory in Cartesian coordinates, where x is horizontal and z is vertical. Time integrating (1) and (2), it follows that the trajectory of the vehicle is described (to first order) by

$$x_{\mathrm{AUV}} = X_0 + Ut - a\frac{\sigma}{\omega} \frac{\cosh[k(Z_0+h)]}{\sinh(kh)} \sin(kX_0 - \omega t) \tag{5}$$

and

$$z_{\mathrm{AUV}} = Z_0 + a\frac{\sigma}{\omega} \frac{\sinh[k(Z_0+h)]}{\sinh(kh)} \cos(kX_0 - \omega t), \tag{6}$$

where ω is the Doppler-shifted frequency, and X_0 and Z_0 denote the initial horizontal position and the mean vertical position of the vehicle, respectively (see details in the appendix). Note that the horizontal velocity of the vehicle relative to the surface wave phase introduces a Doppler shift, $\omega = \sigma - kU$, that modulates the influence of the wave field on the vehicle. This vehicle–wave interaction brings about two processes that lead to a velocity bias in spatially averaged velocity measurements.

First, the vehicle's velocity relative to the waves acts to modify its vertical motion; this is evident from (6). Note that when $U = 0$ and $\omega = \sigma$, the vehicle path matches the orbital trajectory of a fluid parcel at that location, and that the average (over one wave cycle) horizontal velocity measured at the vehicle's location is the Stokes drift velocity. When $U \neq 0$, the vehicle's vertical excursions are modified relative to the fluid trajectory so that the average horizontal velocity measured along the vehicle path then differs from the Stokes drift velocity. We refer to the vehicle path as "quasi Lagrangian," since it includes a component that is related to the Lagrangian Stokes drift but is modified by the vehicle's cruising speed. The spatial average of the quasi-Lagrangian vertical motions then results in a velocity bias in the direction of wave propagation because the vehicle samples faster velocities at the top of its trajectory than it does at the bottom of its trajectory. As $U \to \pm\infty$ and $\omega \to \pm\infty$, the vehicle's speed precludes interactions with the wave field, completely suppressing the amplitude of its vertical motions with $z_{\mathrm{AUV}} \to Z_0$, so the wave-induced bias vanishes.

The second effect arises as a result of changes in temporal sampling of crest versus trough regions. As shown in Fig. 1, the sign of the surface vertical displacement η defines the crest and trough regions. In the vehicle reference frame, the surface wave is described as

$$\eta_{\mathrm{AUV}} = a\cos[kx_{\mathrm{AUV}}(t) - \sigma t], \tag{7}$$

where $x_{\mathrm{AUV}}(t)$ is given by (5). We find the times for the zero crossings, where

$$kx_{\mathrm{AUV}}(t) - \sigma t = \pm\frac{\pi}{2}. \tag{8}$$

Solving for these crossings allows us to compare the vehicle's temporal sampling of crest versus trough regions (see Fig. 2).

An observer at a fixed location (Eulerian perspective) would spend an equal amount of time on either region of the wave. However, the interaction between the vehicle and the wave field acts to prolong the vehicle's time in the crest. Figure 2 shows the fraction of time the vehicle spends under the crest region per wave cycle as a function of the nondimensional vehicle cruising speed. It is observed that the vehicle oversamples the wave crests, thus leading to aliasing of average velocity measurements in the direction of wave travel. This effect becomes more prominent as U increases toward the wave phase speed. A vehicle traveling exactly at the wave phase speed ($u_{\mathrm{AUV}} = c$) would ride on a crest and would thus sample only shoreward motion. As $U \to \pm\infty$, the vehicle–wave interaction becomes inconsequential, and the vehicle spends an equal amount of time in all parts of the wave. Finally, because wave motions decay as a function of depth, the influence of the wave field on the vehicle will be more prominent for sampling routes near the sea surface (Amador et al. 2015).

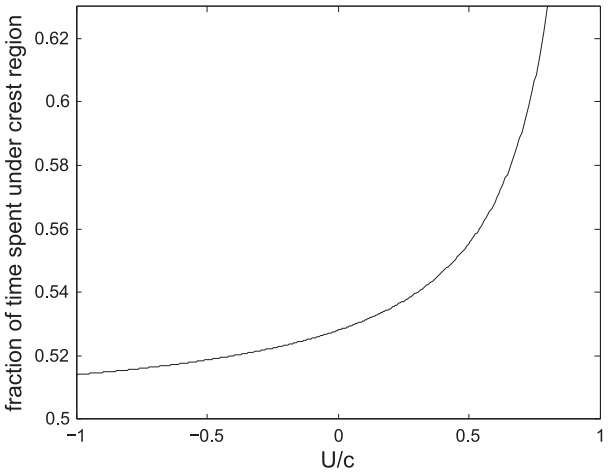

FIG. 2. Fraction of time spent under the crest region of the wave per wave cycle as a function of the nondimensional vehicle cruising speed (U/c), for $Z_0 = -3$ m and local wave conditions: wave amplitude $a = 1$ m, wave period $T = 10$ s, and depth $h = 12$ m.

b. Wave-induced bias

We can now compute the horizontal (u) velocity profile u_{Lq} relative to Earth as measured by an onboard ADCP. This velocity is termed a quasi-Lagrangian measurement, because it is a function of the interaction between the AUV motion and the Lagrangian flow at the AUV position—all extrapolated to the ADCP measurement location. We denote the height of the range cell (above or below the AUV) by Δz. Then

$$u_{\mathrm{Lq}} = u_w[x_{\mathrm{AUV}}(t), z_{\mathrm{AUV}}(t) + \Delta z; t], \tag{9}$$

where the vehicle trajectory, $x_{\mathrm{AUV}}(t)$ and $z_{\mathrm{AUV}}(t)$, is given by (5) and (6). Expanding (9) to include first-order variations in both fluid velocity components and time averaging over one wave cycle (see the appendix), we arrive at the following expression for the wave-induced bias:

$$\overline{u}_{\mathrm{Lq}} = a^2 k \frac{\sigma^2}{\omega} \frac{\cosh[2k(Z_0 + \Delta z + h)]}{2\sinh^2(kh)}. \tag{10}$$

Figure 3 shows the wave-induced bias $\overline{u}_{\mathrm{Lq}}$ normalized by the Stokes drift $\overline{u}_{\mathrm{St}}$ at the vehicle depth Z_0 for different vehicle velocities in deep-water waves with period $T = 10$ s. The black dashed line illustrates the solution of (10) when $U = 0$, the gray dashed line represents the nondimensional depth of the vehicle, and the gray bold line shows the normalized Stokes drift profile. As expected, the measured velocity matches the Stokes drift at the vehicle's depth (i.e., $\overline{u}_{\mathrm{Lq}}/\overline{u}_{\mathrm{St},z_0} = 1$) when $U = 0$. However, the measured profile deviates from Stokes drift with varying depth because the velocity at each depth is sampled using particle paths at the vehicle depth, which differ from the local particle paths that result in the actual vertical variation in the Stokes drift (Amador et al. 2015). In other words, for $U = 0$, the wave-induced bias is greater than the Stokes drift below Z_0 because the orbital paths of the range cells are greater than the particle orbits below the vehicle depth. The opposite is true for velocity measurements obtained above Z_0.

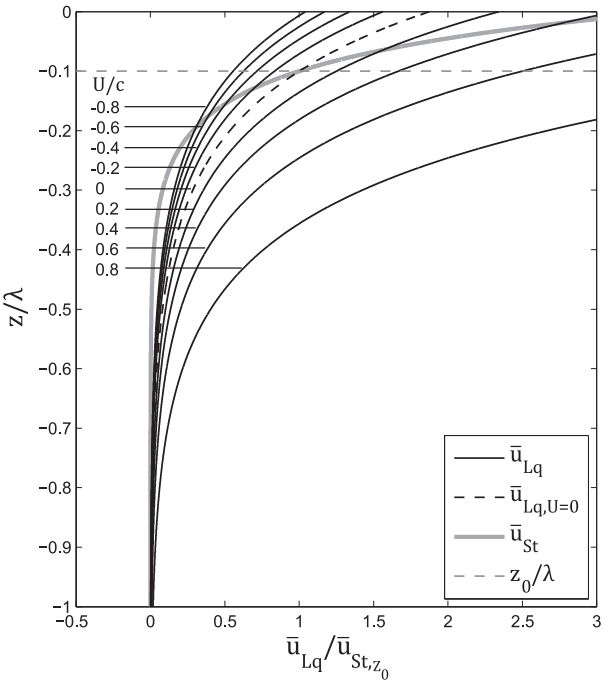

FIG. 3. Wave-induced bias $\overline{u}_{\mathrm{Lq}}$ (black lines) as a function of nondimensional depth (z/λ) for different vehicle velocities in deep-water waves with period $T = 10$ s. Normalized wave-induced bias when $U = 0$ (black dashed line), normalized Stokes drift profile $\overline{u}_{\mathrm{St}}$ (gray thick line), and the nondimensional depth of the vehicle (gray dashed line). Results have been normalized by $\overline{u}_{\mathrm{St}}$ at the vehicle depth ($Z_0/\lambda = 0.1$).

As discussed in section 2a, the vehicle's horizontal velocity relative to the wave phase modifies the wave-induced bias—the solid black lines presented in Fig. 3 illustrate this effect. Note that the wave-induced bias is enhanced when the vehicle moves in the direction of wave propagation ($U > 0$) because the Doppler-shifted frequency decreases. Conversely, when the vehicle moves against the waves ($U < 0$), the Doppler frequency increases and the wave-induced bias is diminished.

3. Field data

We present data from AUV hydrodynamic surveys over coral reefs at two different locations off the coast of Oahu, Hawaii. The description of the field observations

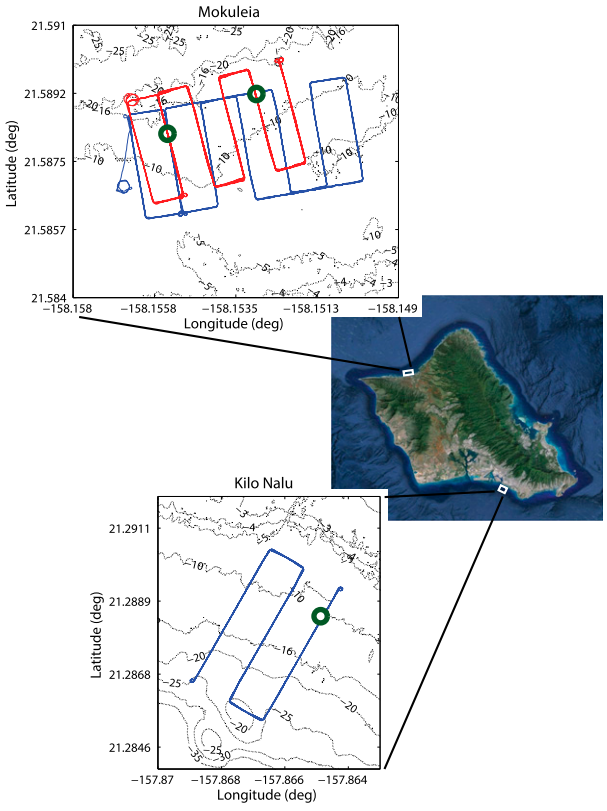

FIG. 4. Study area and survey regions overlaid with lidar bathymetry. Tracks followed by the AUV during the hydrodynamic surveys (red and blue lines). Location of the upward-looking fixed ADCPs (bold green circles).

in the next two paragraphs follows from Amador et al. (2015) with minor modifications.

Field experiments were carried out near Mokuleia and at the Kilo Nalu Oahu Reef Observatory (Pawlak et al. 2009), located on the north and south shores of Oahu, respectively. The location of the study sites and the bathymetry of the survey regions are shown in Fig. 4. Currents are predominantly alongshore and vary semidiurnally on both reef systems. Observations at each site include a series of AUV surveys targeting the spatial structure of the flow field and water properties (temperature, salinity, optical backscatter). Each study site featured bottom-mounted, upward-looking four-beam 1200-kHz RD Instruments Workhorse ADCPs deployed at depths in the range of 11–13 m and located within the AUV survey domain. The fixed ADCPs were programmed to sample in 0.25-m bins with a blanking distance of 0.5 m, and measured velocity profiles and bottom pressure at 1 Hz. Wave conditions for each set of observations were dominated by narrowbanded long-period swell with light winds and minimal short-period wave energy. The observations span a range of wave heights for which the theoretically predicted bias effects $\overline{u}_{\mathrm{Lq}}$ vary significantly. Key parameters have been summarized in Table 1.

AUV surveys consisted of mow patterns in both along- and cross-shore directions spanning a significant portion of the tidal cycle. To assess DVL performance, each survey included legs in opposite directions, measuring water velocities in close proximity to fixed-point current measurements gathered by upward-looking ADCPs. REMUS DVLs were configured to sample in 1-m bins with a blanking distance of 1 m and a sampling frequency of approximately 0.67 Hz. The vehicle was programmed to maintain an average depth of 3 and 2 m below the surface for the Kilo Nalu and the Mokuleia experiments, respectively, as described in Table 1. For all the experiments, the vehicle was set to cruise at a velocity of $2\,\mathrm{m\,s^{-1}}$.

a. *Fixed ADCP data*

To understand how the fixed ADCP averaging interval affects the analysis, we examined a series of depth-averaged velocity realizations centered on AUV transect times. Figure 5a shows the RMSD of depth-averaged, nondimensional velocity differences,

$$\left(\frac{\overline{V}_{\bar{t}}-\overline{V}_{20}}{V_{\sigma}}\right)_{\mathrm{RMSD}}=\sqrt{\frac{1}{N}\sum_{i=1}^{N}\left(\frac{\overline{V}_{\bar{t}}-\overline{V}_{20}}{V_{\sigma}}\right)_{i}^{2}}, \quad (11)$$

in the direction of wave propagation as a function of nondimensional time $\bar{t}/T_p$. Here, T_p represents the observed peak wave period for each 20-min window, $\bar{t}$ is a varying interval for time averaging, $\overline{V}_{20}$ is the time-averaged velocity over a 20-min interval, and N is the number of ensembles. Normalizing by the velocity standard deviation of each 20-min realization V_{σ} accounts for the effects of varying wave conditions. The underlying assumption here is that for Eulerian measurements (such as fixed ADCP measurements), a $\bar{t}=20$-min averaging interval can effectively eliminate the influence of the wave velocities on the mean velocity.

We further compare the RMSD values to estimates of the expected uncertainty in time-averaged, fixed ADCP velocity measurements in Fig. 5a. Errors in the ADCP measurements are expected to be normally distributed about the mean flow. The expected uncertainty is calculated as a wave-induced uncertainty normalized by the standard deviation of the velocity for each 20-min realization. The wave-induced uncertainty is estimated by dividing the standard deviation of the velocity (dominated by wave motion for these data) for each time window by the square root of the effective degrees

TABLE 1. Local wave conditions and transect information.

Experiment	Deployment dates	H_{sig} (m)	T_p (s)	D_p (°)	No. transects	AUV orientation (°)	AUV depth (m)	Local depth (m)
Kilo Nalu I (cross-shore)	29 Jun 2010	0.8	11.4	206	7 shoreward 8 seaward	30 210	2.9	11.7
Kilo Nalu II (cross-shore)	6 Jul 2010	0.8	9.7	171	7 shoreward 8 seaward	30 210	2.9	11.3
Mokuleia I (cross-shore)	11 Dec 2010	1.2	11.2	349	8 shoreward 7 seaward	170 350	1.9	12.7
Mokuleia II (alongshore)	11 Dec 2010	1.3	11.0	351	8 upcoast 7 downcoast	79 261	1.9	13.0
Mokuleia III (cross-shore)	15 Dec 2010	1.3	12.2	346	7 shoreward 13 seaward	166 345	1.9	13.2
Mokuleia IV (cross-shore)	15 Dec 2010	1.4	12.7	345	7 shoreward 7 seaward	164 345	1.9	11.2
Mokuleia V (cross-shore)	17 Dec 2010	0.8	10.2	349	7 shoreward 13 seaward	162 345	1.9	12.8
Mokuleia VI (cross-shore)	17 Dec 2010	0.7	10.3	344	7 shoreward 7 seaward	164 345	1.9	10.9

of freedom. Degrees of freedom are calculated using an estimated integral time scale (see Emery and Thomson 1997). Note that the wave-induced uncertainty implicitly includes random instrument errors that can be estimated by computing the standard deviation of the error velocity (single-ping error), and should decay with the square root of the number of measurements being averaged (Gordon 1996).

Ideally, the ADCP averaging interval should be comparable to the AUV transect times (1–2 min) and should eliminate wave orbital velocities. As evidenced in Fig. 5a, wave velocities are significantly suppressed within the first few wave cycles. We see that the expected uncertainty estimate (dashed gray line) captures the behavior of the RMSD values (solid black line), indicating that the observed deviations are adequately described by normally distributed measurement errors associated with random instrument noise and wave-induced uncertainties.

ADCP-derived velocity profiles used in our calculations were time averaged over an interval of $\bar{t} = 10T_p$ (~1.5–2.5 min). Here, random instrument errors are negligible in the uncertainty estimate because wave velocities (V_σ ~12–25 cm s^{-1}) are an order of magnitude greater than the ADCP single-ping error (~2 cm s^{-1}), and because the effective number of degrees of freedom is always less than the number of measurements. Based on this analysis, we expect fixed ADCP errors to be in the range from ~0.7 to ~2 cm s^{-1}, depending on wave conditions.

b. AUV data

AUV-based velocity measurements rely on spatiotemporal averaging to reduce noise and to obtain useful estimates of the current velocities. However, it is not immediately clear what the adequate averaging length should be, especially when averaging under the influence of nonmonochromatic waves. To examine the effects of spatial averaging, depth-averaged velocity differences ($\Delta\overline{V} = \overline{V}_{AUV} - \overline{V}_{ADCP}$) were calculated in a cross- and along-track reference frame and as a function of the averaging length $\overline{L}$. We focus below on the standard deviation and the expected uncertainty of these velocity differences over multiple transects to identify an optimal averaging length. It should be noted that the averaging length is limited by total transect length and that velocities calculated over very long averaging lengths may suffer from changes caused by spatial variability.

Figure 5b shows the RMSD of depth-averaged, nondimensional velocity differences,

$$\left(\frac{\Delta\overline{V}}{V_\sigma}\right)_{RMSD} = \sqrt{\frac{1}{N}\sum_{i=1}^{N}\left(\frac{\Delta\overline{V}}{V_\sigma}\right)_i^2}, \tag{12}$$

with solid black lines and estimates of the total expected uncertainty with dashed gray lines for all cross-shore transects N as a function of nondimensional averaging length $\overline{L}/\lambda_{eff}$. The effective wavelength λ_{eff} was calculated for each transect using the corresponding Doppler-shifted peak wave frequency. ADCP-derived, time-averaged velocities $\overline{V}_{ADCP}$ and V_σ were calculated for each transect over an interval of 10 peak wave periods. As noted in section 3a, normalizing by the ADCP-derived standard deviations accounts for the effects of varying wave conditions.

The total expected uncertainty is calculated as the square root of the sum of the squares (RSS) of the fixed ADCP measurement uncertainty (over 10 wave periods) and the AUV measurement uncertainty,

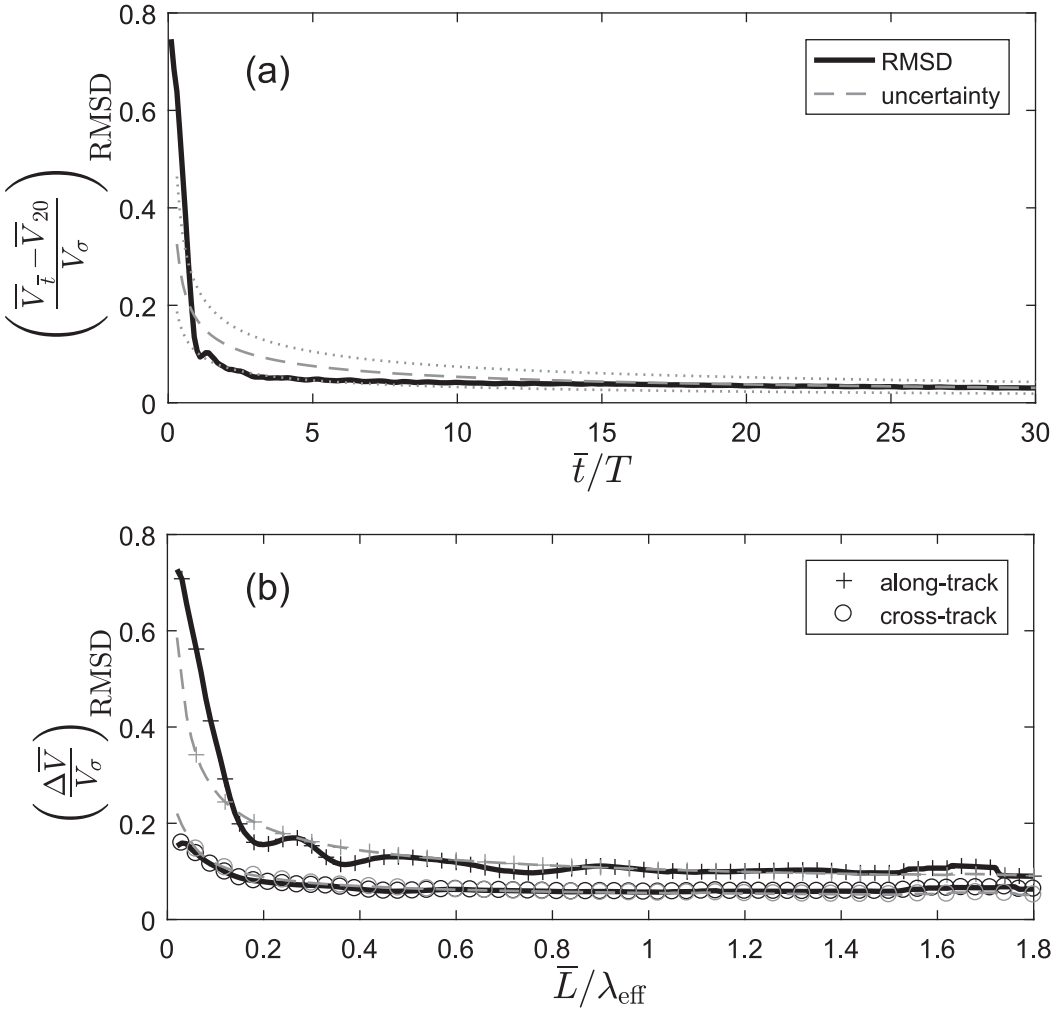

FIG. 5. (a) RMSD of depth-averaged, fixed ADCP velocity differences, normalized by the wave velocity standard deviations (solid black line) and expected uncertainty estimates (dashed gray line) as a function of $\bar{t}/T_p$. Standard deviation of the expected uncertainty estimates (gray dotted lines). (b) RMSD values of nondimensional, depth-averaged velocity differences (solid black lines) and expected uncertainty estimates (dashed gray lines) for all cross-shore transects as a function of $\overline{L}/\lambda_{\text{eff}}$. Cross-track (circles) and along-track (crosses) quantities.

normalized by the wave velocity standard deviation. Similar to the fixed ADCP uncertainty, the AUV measurement uncertainty implicitly includes random DVL errors and is similarly calculated as the wave-induced uncertainty divided by the square root of the effective number of degrees of freedom. Again, the wave-induced uncertainties are typically one order of magnitude greater than random DVL errors because the velocity standard deviations ($\sim$10–26 cm s^{-1}) measured by the AUV are significantly larger than DVL single-ping errors ($\sim$4 cm s^{-1}), and the effective number of degrees of freedom is always less than the number of measurements.

As seen in Fig. 5b, the RMSD and the expected uncertainty of the along-track velocity differences decay within one effective wavelength ($\overline{L} \sim \lambda_{\text{eff}}$), consistent with the reduction of wave-induced velocities via spatial averaging. Note that both the RMSD values and the expected uncertainty of the velocity differences are significantly lower in the cross-track direction because for cross-shore transects the wave field is generally aligned in the along-track direction. Furthermore, the RMSD values of the cross- and along-track differences level off as the relative averaging length increases, indicating a "minimum uncertainty" in our measurements. This feature, whose minimum is bounded by the fixed ADCP measurement uncertainty (at 10 peak wave periods), is also captured by the expected uncertainty estimate, suggesting that normally distributed measurement errors associated with wave-induced uncertainties are

responsible for the observed behavior. In addition, we note that spatial variations as a result of shear and turbulence along the vehicle track may play a more prominent role in the measurement uncertainty with increasing averaging lengths, as progressively larger scales begin to affect the RMS velocities.

Based on this analysis, AUV-based velocity profiles were calculated over an $\overline{L}$ equivalent to λ_{eff}. The effective wavelength ranged from ~110 to ~180 m, depending on the velocity of the AUV relative to the waves and the local conditions. The estimated uncertainties ranged from ~1.8 to ~4.5 cm s^{-1} per transect for the along-track velocity differences and ~0.8 to ~1.5 cm s^{-1} per transect for the cross-track velocity differences in cross-shore transects. AUV-based velocity profiles were obtained using the downward-looking DVL and centered at fixed ADCP locations (within ~10 m) in all datasets.

c. *Wave spectra*

The wave-induced bias calculated in (10) for monochromatic waves can be more accurately calculated considering a spectral distribution of the wave field $S_{\eta\eta}$, so the quasi-Lagrangian velocity is rewritten as

$$\overline{u}_{\text{Lq}} = \int_{f_a}^{f_b}\int_{\theta_a}^{\theta_b} k\frac{\sigma^2}{\omega}\frac{\cosh[2k(Z_0+\Delta z+h)]}{\sinh^2(kh)}S_{\eta\eta}\,d\theta\,df, \quad (13)$$

where

$$\int_0^{\infty}\int_{-\pi}^{\pi} S_{\eta\eta}(f,\theta)d\theta\,df = \langle\eta^2\rangle \quad (14)$$

and the angle brackets $\langle\rangle$ denote an ensemble-averaging operator. Here, $f_a = 0.03$ Hz and $f_b = 0.5$ Hz represent the limits of the sea-swell frequency band under consideration; θ defines the direction of wave propagation; and $\theta_b - \theta_a = \pi/3$, centered on the transect mean orientation. The extended maximum entropy method (EMEP) (Hashimoto 1997) was used to estimate directional wave spectra from fixed ADCP data (10-min pressure and velocity time series).

4. Analysis and results

To investigate bias errors in AUV-based measurements, spatially averaged ($\overline{L} = \lambda_{\text{eff}}$) velocity profiles were calculated using downward-looking DVL data and rotated into along- and cross-track components for each transect (Amador et al. 2015). ADCP-derived velocity profiles were time averaged ($\overline{t} = 10T_p$) and also rotated into along- and cross-track components. Velocity differences ($\Delta V = V_{\text{AUV}} - V_{\text{ADCP}}$) were calculated over a range of depths above the fixed ADCPs' first range cell and excluded regions near boundaries (11% of range to boundary) to avoid acoustic sidelobe interference issues. The wave-induced bias $\overline{u}_{\text{Lq}}$ was calculated using a fixed ADCP-derived directional spectrum as described in section 3c.

We focus below on an example drawn from two sets of transects gathered at the Mokuleia study site on 11 December 2010. Figure 6 shows ensemble-averaged velocity differences ($\langle\Delta V\rangle = \langle V_{\text{AUV}} - V_{\text{ADCP}}\rangle$) for 14 cross-shore (Figs. 6a,b) and 14 alongshore (Figs. 6c,d) transects. The expected wave-induced bias $\overline{u}_{\text{Lq}}$, calculated using (13), has also been plotted here for reference.

Considering the effects of a wave-induced bias only, we anticipate that $\langle\Delta V\rangle \approx \pm\overline{u}_{\text{Lq}}$ when the measured velocity component is aligned with the direction of wave propagation. Here, the relative wave direction determines the sign of $\overline{u}_{\text{Lq}}$. The wave-induced bias should be zero for velocity components that are perpendicular to the direction of wave propagation.

The top panels in Fig. 6 show the observed velocity differences for along-track (Fig. 6a) and cross-track (Fig. 6b) components in cross-shore transects. For the shoreward legs, the observed along-track ΔV profiles (Fig. 6a) show a positive bias that exceeds the predicted wave-induced bias. The seaward legs exhibit a weaker, slightly positive bias. A comparison between the measured and the expected values (dashed lines in Fig. 6a) reveals that both ΔV profiles lie to the right of the theoretical prediction. In other words, REMUS-based velocity measurements show a bias in the direction of vehicle motion relative to the wave-induced bias; we refer to this deviation as the forward residual bias ($V_{\text{res}} = \Delta V - \overline{u}_{\text{Lq}}$). As expected, the observed cross-track velocity differences (Fig. 6b) in both shoreward and seaward transects do not show an appreciable bias. Vector diagrams in Fig. 7a illustrate the observed ΔV in cross-shore transects as vector sums of $\overline{u}_{\text{Lq}}$ and residual velocities V_{res}.

The bottom panels in Fig. 6 show the observed along-track (Fig. 6c) and cross-track (Fig. 6d) velocity differences in alongshore transects. Measurements of cross-track ΔV for alongshore transects (Fig. 6d) are well predicted by the theoretical model with wave-induced biases appearing in the direction of wave travel for both upcoast (westward for Mokuleia) and downcoast transects (eastward for Mokuleia). For the along-track velocity component (Fig. 6c), however, a forward bias appears for both transect directions that is unaccounted for by wave bias theory. Vector diagrams again summarize the contributions of the wave-induced and forward residual biases for the alongshore transects in Fig. 7b.

The results observed in Fig. 6 are representative of experiments conducted in a range of current and wave conditions (see Table 1) at both field sites. Figure 8

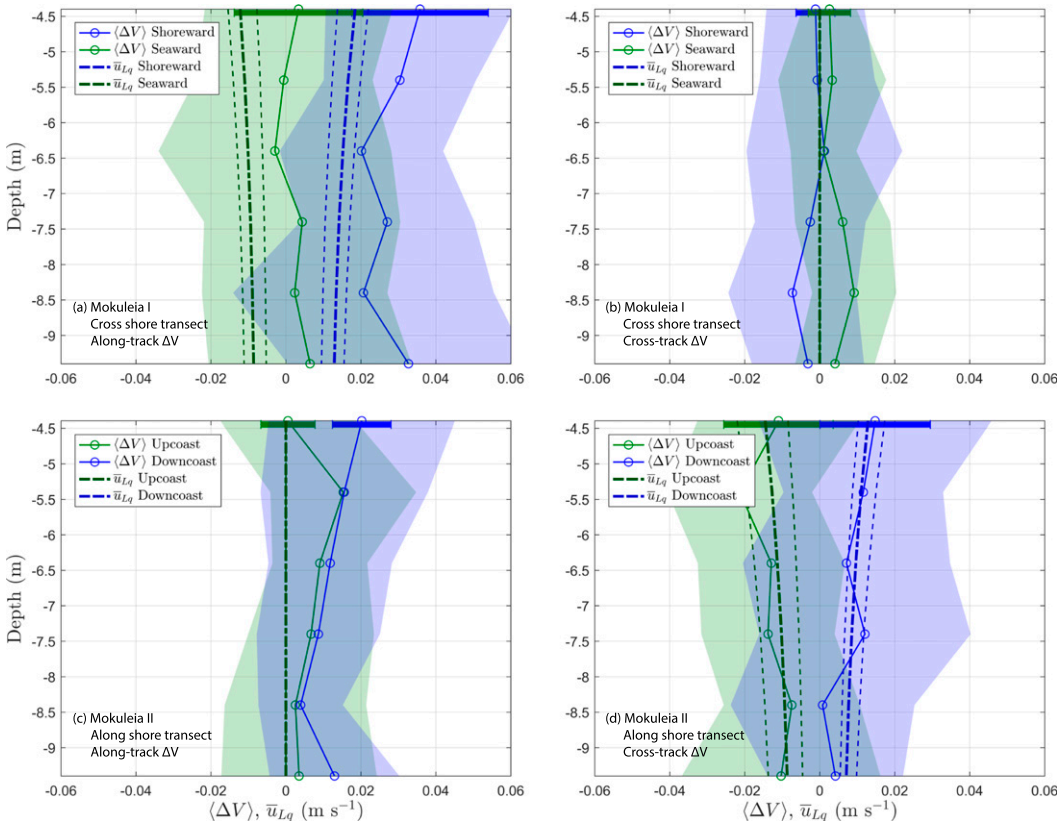

FIG. 6. Ensemble-averaged velocity differences ($\langle \Delta V \rangle = \langle V_{\mathrm{AUV}} - V_{\mathrm{ADCP}} \rangle$) and $\overline{u}_{\mathrm{Lq}}$ on a cross- and along-track reference frame. Shaded error bands represent one standard deviation of the velocity difference, and solid error bars at the top of each profile indicate the calculated uncertainties (similar at all depths) in the ensemble-averaged profiles. Range of values used when calculating $\overline{u}_{\mathrm{Lq}}$ for each individual transect (thin dashed lines).

shows depth-averaged velocity differences as a function of the theoretical along-track, depth-averaged wave-induced bias for all cross-shore transects considered in this study. Gray dots and black crosses illustrate individual transects and mission ensemble averages, respectively. The black dashed line in Fig. 8a depicts a one-to-one relationship ($\Delta\overline{V} = \overline{u}_{\mathrm{Lq}}$) for reference. In the left panel (Fig. 8a), we see that the ensemble-averaged data points lie above the one-to-one relationship (i.e., along-track velocity differences exceed the theoretically expected values). In contrast, the right panel (Fig. 8b) shows the cross-track velocity differences for all cross-shore transects. In spite of the scatter in individual measurements, it is evident that the average cross-track velocity differences in both shoreward and seaward transects do not show an appreciable bias.

5. Discussion

The theory presented here describes the motion of a vehicle within a spectral wave field and the implications of quasi-Lagrangian dynamics on AUV-based velocity measurements. The resulting effect is related to Stokes drift, but it is modified by the vehicle's velocity relative to the wave speed. In this case, the wave-induced motions lead to vertical oscillations of the AUV and of the DVL sampling volumes, with preferential sampling of the crest regions; this results in a velocity bias in the direction of wave propagation. Observations show significant biases that are dependent on relative wave direction, in agreement with the predictions of the theory, but also reveal the presence of a persistent offset in the direction of vehicle motion. This residual forward bias is consistent with observations in other studies (e.g., Fong and Monismith 2004; Fong and Jones 2006; Jaramillo and Pawlak 2010), which have also reported a forward velocity bias in both AUV and shipboard measurements even in the absence of waves.

The clearest illustration of the residual bias ($V_{\mathrm{res}} = \Delta V - \overline{u}_{\mathrm{Lq}}$) is apparent in the along-track, alongshore velocity shown in Fig. 6c. Here, the wave direction is perpendicular to the vehicle track, and the residual velocity is persistently in the direction of vehicle motion (along-track positive for all plots in Fig. 6). Furthermore,

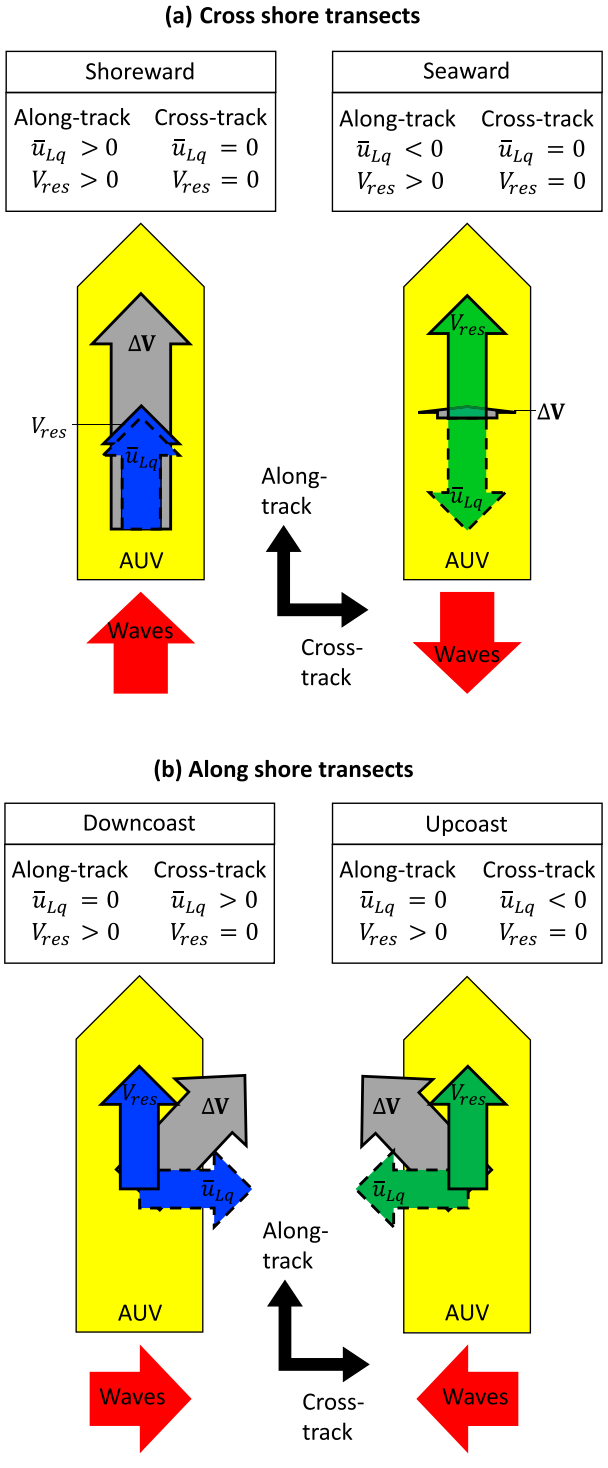

FIG. 7. Observed velocity difference vector $\mathbf{\Delta V}$ and bias components ($\bar{u}_{\mathrm{Lq}}$, V_{res}) in a cross- and along-track reference frame for (a) cross- and (b) alongshore transects. Bias velocity components are shown in blue (shoreward and downcoast legs) and green (seaward and upcoast legs) as in Fig. 6.

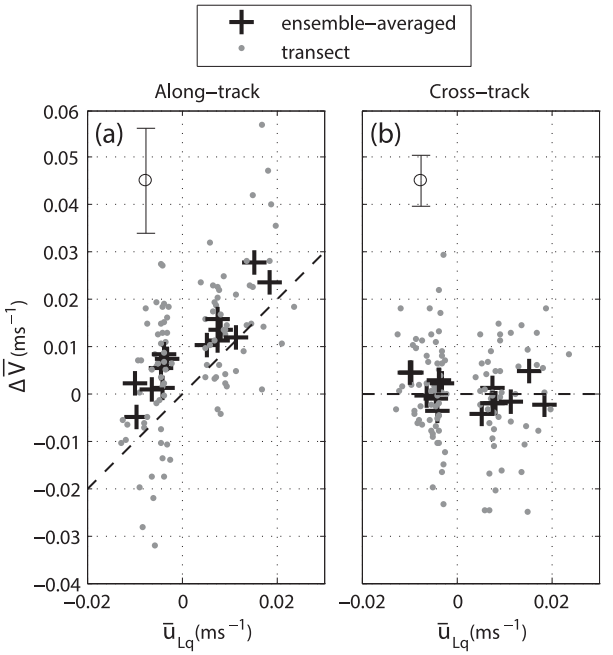

FIG. 8. Depth-averaged velocity differences $\Delta\overline{V}$ as a function of the expected along-track $\bar{u}_{\mathrm{Lq}}$ for all cross-shore transects considered in this study. Vertical error bars at the top-left corner represent the average along- and cross-track uncertainty estimate of all ensembles.

results in Fig. 8 confirm the presence of a residual bias that is independent of the relative wave direction. We can conclude therefore that the forward residual bias is associated with a separate process independent of the wave-induced bias described by the theory.

a. Forward residual bias

The residual bias in the direction of vehicle motion warrants a closer inspection of the bottom-tracking velocity estimates. An underestimation of the vehicle velocity by the bottom-tracking system could lead to the observed forward velocity bias in the along-track velocity measurements. This was examined and dismissed by Fong and Monismith (2004) by comparing bottom-tracking velocities with real-time kinematic (RTK) GPS position estimates. Here, because the vehicle is submerged, GPS positioning is not available. Bottom-track velocities were compared with velocities derived from the LBL navigation system, following Joyce (1989). Averaged over transects, differences between bottom-tracking and LBL velocities showed no correlation with transect-averaged velocity differences, ΔV, indicating that bottom-tracking errors are not responsible for the observed biases.

The forward residual bias is shown in Fig. 9 as a function of the vertical distance from the vehicle (range)

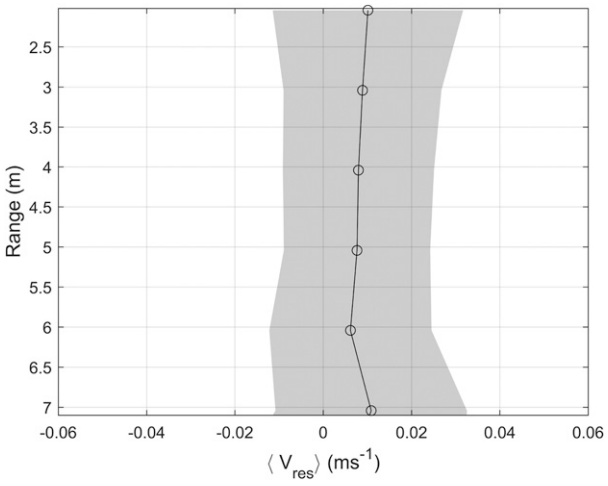

FIG. 9. Average residual bias obtained by removing the wave-induced bias from the along-track velocity differences ($\langle V_{\rm res}\rangle = \langle \Delta V - \overline{u}_{\rm Lq}\rangle$). Sample standard deviation is shown by the shaded region.

based on an ensemble-average of along-track velocity differences for the entire dataset. Although the scatter is notable, the profile shows a bias of $\sim$1 cm s^{-1} that is fairly uniform with distance from the transducer, over the range considered. It is possible that acoustic ''ringing'' of the DVL mount may be responsible, at least in part, for the observed residual bias. Ringing occurs when the transmitted pulse excites the transducer head and causes it to resonate at the transmit frequency. The DVL then processes both the return signal from the water and the ringing signal biasing the velocity data in the direction of the vehicle motion. In this case, one would expect a forward residual bias that is proportional to the vehicle velocity.

Conclusive confirmation of the source for the residual bias would require extensive additional surveys to be conducted at varying vehicle speeds and in greater depths in order to resolve a dependence on platform velocity over a longer profile. With a relatively narrow range of practical cruising speeds (1–2 m s^{-1} for the REMUS 100), a large number of repeated transects would be needed at each speed to sufficiently reduce measurement uncertainties. For the present dataset, it was not possible to verify acoustic ringing as an explanation for the additional bias, since vehicle speeds were maintained at 2 m s^{-1}. Acoustic ringing effects are expected be intensified near the transducer, which should lead to a decaying bias profile. For the low backscatter tropical reef environment, the decay rate would likely be weaker, however.

In addition to ringing and bottom-tracking errors, a velocity bias error can occur due to a misalignment between the DVL and the forward axis of the vehicle. Misalignment errors, estimated following Joyce (1989), were found to be negligible. Other potential sources for error in ADCP measurements include spatial and temporal variations in velocity (shear, turbulence, waves), errors in instrument orientation (pitch, roll, heading), sidelobe interference, variations in sound speed, Doppler noise, velocity ambiguity errors, and timing errors (González-Castro and Muste 2007). These error sources were dismissed as sources of persistent bias, since they either contribute to random error or they are not applicable to the AUV configuration.

b. *Additional comments*

The analysis of the wave-induced bias assumes that the AUV follows the wave motion closely, neglecting any relative inertia. In reality, AUV motion will deviate from the wave motion for higher frequencies. A comparison of pressure spectra measured by the vehicle and the fixed ADCPs for the observations presented earlier indicated that the vehicle follows closely the dominant motions produced by the spectral wave field. Field data show that the dominant spectral energy content was typically confined to a narrow band within the range of 10 s $\lesssim T \lesssim$ 15 s for all observations. Shorter-period wave energy was minimal, although the analysis reveals that the vehicle begins to deviate from the wave motions for wavelengths smaller than around 60 m ($\lambda \approx 60$ m, $T \approx 7$ s, for $h \approx 11$ m), suggesting that the vehicle's inertia will play a role in partially filtering the higher-frequency waves.

Although small O(1–5) cm s^{-1}, the wave-induced and residual biases are not inconsequential and can be comparable to water velocities associated with steady and low-frequency flow features. For example, bias errors may be significant when measuring cross-shore exchange flows and attempting to resolve the spatial structure of vortical features in the inner shelf, where flow speeds may be on the order of 1–10 cm s^{-1}. Also, velocity biases may affect the measurement of horizontal velocity shears, complicating the calculation of flow parameters such as vorticity, salt and momentum fluxes, and the Richardson number (Fong and Monismith 2004).

In principle, the wave-induced bias can be corrected, provided that the in situ wave field is known. Here, we provide wave-induced bias estimates based on only directional wave spectra measured by bottom-mounted, fixed ADCPs in close proximity to the AUV and over a time window that exceeds the AUV averaging time. However, recent work by Haven and Terray (2015) has shown that it is possible to measure sea surface spectra and mean wave direction from an underway AUV equipped with an onboard ADCP and inertial sensors. This new capability could provide a more accurate way

to measure and correct for the wave-induced bias in AUV-based measurements, with the additional advantage of being independent of supplementary wave information. In the absence of field measurements, modeled wave conditions can provide an estimate of the sea surface spectra.

6. Summary

The trajectory for a small AUV moving under surface waves can be altered due to the interactions between the vehicle and the wave field. These changes in trajectory introduce a quasi-Lagrangian bias in AUV-based velocity measurements that is related to Stokes drift.

Here, we have developed a theoretical framework to describe the motion of the AUV within a spectral wave field based on a first-order expansion of the linear wave solution. Using this framework we quantify the wave-induced bias as a function of the local wave conditions, and the vehicle's depth and velocity. The analysis shows that the vehicle's velocity relative to the wave phase speed acts to enhance or suppress the bias mechanism by modifying the vehicle's vertical excursions and its relative spatiotemporal sampling of trough versus crest regions.

Theoretical predictions are in good agreement with observations from AUV surveys carried out in conjunction with current velocity measurements from bottom-mounted ADCPs. AUV-based velocity profiles were calculated over an averaging length equivalent to the effective wavelength (λ_{eff} ~110–180 m) and compared with time-averaged ($10T_p$ ~1.5–2.5 min), fixed ADCP measurements. Ensemble-averaged velocity differences ($\langle \Delta V \rangle = \langle V_{\text{AUV}} - V_{\text{ADCP}} \rangle$) calculated in a cross- and along-track reference frame, and obtained in a range of wave conditions confirm the presence of a wave-induced bias consistent with theory but also reveal an additional, persistent bias in the direction of the vehicle motion that is unaccounted for by wave effects. It is speculated that the unexplained residual may be associated with acoustic ringing effects. Together, the bias errors are comparable in magnitude to steady flow velocities for inner-shelf regions and thus must be considered for AUV-based measurements in these environments.

Acknowledgments. This work was carried out with funding from the Office of Naval Research, via Awards N00014-13-1-0340 and N00014-12-1-0221. The authors thank Mark Merrifield, Carly Fetherolf, Chris Kontoes, Chris Colgrove, and Kimball Millikan for their assistance with field operations in support of the work described here. Eugene Terray provided valuable feedback in the development of the theoretical model. The manuscript also benefited from the helpful suggestions of three anonymous reviewers. A preliminary version of the work described here was originally presented at the IEEE/OES 11th Current, Waves and Turbulence Measurement Workshop (CWTM) held in St. Petersburg, Florida, on 3 March 2015, and appeared in the unrefereed conference proceedings (Amador et al. 2015).

APPENDIX

Wave-Induced Bias

A theoretical model is developed to describe the wave-induced bias observed in AUV-based velocity measurements. Here we assume that the vehicle follows very closely the horizontal and vertical water displacements produced by surface gravity waves.

a. AUV trajectory

Consider deep-water surface gravity waves as given by linear wave theory:

$$u_w = a\sigma e^{kz}\cos(kx - \sigma t) \quad \text{and} \tag{A1}$$

$$w_w = a\sigma e^{kz}\sin(kx - \sigma t) \tag{A2}$$

in Cartesian coordinates where x is horizontal and z is vertical. Here u_w and w_w specify the horizontal and vertical wave velocities, respectively; a is the wave amplitude; σ is the wave radian frequency; and k is the wavenumber. The trajectory of a particle immersed in a monochromatic wave field can be obtained by solving the following set of ordinary differential equations:

$$\frac{dx}{dt} = U + a\sigma e^{kz}\cos(kx - \sigma t) \quad \text{and} \tag{A3}$$

$$\frac{dz}{dt} = a\sigma e^{kz}\sin(kx - \sigma t) \tag{A4}$$

with initial conditions $x(0) = X_0$ and $z(0) = Z_0$. We define the nondimensional variables as

$$\hat{x} = kx, \quad \hat{z} = kz, \quad \hat{t} = \sigma t, \tag{A5}$$

and the nondimensional problem is then

$$\frac{d\hat{x}}{d\hat{t}} = \frac{U}{c} + \varepsilon e^{\hat{z}}\cos(\hat{x} - \hat{t}) \quad \text{and} \tag{A6}$$

$$\frac{d\hat{z}}{d\hat{t}} = \varepsilon e^{\hat{z}}\sin(\hat{x} - \hat{t}), \tag{A7}$$

where $c = \sigma/k$ is the wave phase speed and the small parameter $\varepsilon = ak \ll 1$ is the wave steepness.

We analyze this problem using a regular perturbation series expansion,

$$\hat{x} = \hat{x}_0 + \varepsilon\hat{x}_1 + \varepsilon^2\hat{x}_2 + \cdots \quad \text{and} \tag{A8}$$

$$\hat{z} = \hat{z}_0 + \varepsilon\hat{z}_1 + \varepsilon^2\hat{z}_2 + \cdots. \tag{A9}$$

At leading order, we have

$$\frac{d\hat{x}_0}{d\hat{t}} = \frac{U}{c}, \quad \text{with solution} \quad \hat{x}_0 = \frac{U}{c}\hat{t} + \hat{X}_0, \quad \text{and} \tag{A10}$$

$$\frac{d\hat{z}_0}{d\hat{t}} = 0, \quad \text{with solution} \quad \hat{z}_0 = \hat{Z}_0. \tag{A11}$$

At the next order,

$$\frac{d\hat{x}_1}{d\hat{t}} = e^{\hat{z}_0}\cos(\hat{x}_0 - \hat{t}), \tag{A12}$$

$$= e^{\hat{Z}_0}\cos\left[\hat{X}_0 - \left(1 - \frac{U}{c}\right)\hat{t}\right], \quad \text{and} \tag{A13}$$

$$\hat{x}_1 = -\frac{1}{1 - U/c}e^{\hat{Z}_0}\sin\left[\hat{X}_0 - \left(1 - \frac{U}{c}\right)\hat{t}\right]. \tag{A14}$$

Similarly,

$$\frac{d\hat{z}_1}{d\hat{t}} = e^{\hat{z}_0}\sin(\hat{x}_0 - \hat{t}), \tag{A15}$$

$$= e^{\hat{Z}_0}\sin\left[\hat{X}_0 - \left(1 - \frac{U}{c}\right)\hat{t}\right], \quad \text{and} \tag{A16}$$

$$\hat{z}_1 = \frac{1}{1 - U/c}e^{\hat{Z}_0}\cos\left[\hat{X}_0 - \left(1 - \frac{U}{c}\right)\hat{t}\right]. \tag{A17}$$

Substituting the solutions for $\hat{x}_0$, $\hat{x}_1$, $\hat{z}_0$, and $\hat{z}_1$ in our regular perturbation expansion [(22), (23)], we get

$$\hat{x} = \hat{X}_0 + \frac{U}{c}\hat{t} - \frac{\varepsilon}{1 - U/c}e^{\hat{Z}_0}\sin\left[\hat{X}_0 - \left(1 - \frac{U}{c}\right)\hat{t}\right] + O(\varepsilon^2) \quad \text{and} \tag{A18}$$

$$\hat{z} = \hat{Z}_0 + \frac{\varepsilon}{1 - U/c}e^{\hat{Z}_0}\cos\left[\hat{X}_0 - \left(1 - \frac{U}{c}\right)\hat{t}\right] + O(\varepsilon^2). \tag{A19}$$

Using dimensional variables, the vehicle trajectory is

$$x = X_0 + Ut - a\frac{\sigma}{\omega}e^{kZ_0}\sin(kX_0 - \omega t) \quad \text{and} \tag{A20}$$

$$z = Z_0 + a\frac{\sigma}{\omega}e^{kZ_0}\cos(kX_0 - \omega t), \tag{A21}$$

where $\omega = \sigma - kU$ is the Doppler-shifted frequency.

b. AUV-based velocity measurements

We can now compute the mean u velocity profile relative to Earth as measured by an onboard ADCP, u_{Lq}. We use Δz to denote the height of the range cell (above or below the AUV). Then

$$u_{\mathrm{Lq}} = u_w[x(t), z(t) + \Delta z; t], \tag{A22}$$

where $x(t)$ and $z(t)$ describe the vehicle's trajectory. Again, for simplicity, we assume deep-water waves,

$$u_{Lq} = a\sigma e^{k[z(t)+\Delta z]}\cos[kx(t) - \sigma t]. \tag{A23}$$

To solve for the time-averaged velocity profiles, we use a Taylor series expansion to include first-order variations in both fluid velocity components and time average over one wave cycle (indicated here by the overbar),

$$\overline{u}_{\mathrm{Lq}} = \overline{u_{\mathrm{Lq}}(X_0, Z_0; t)} + \overline{(x - X_0)\frac{\partial u_{\mathrm{Lq}}}{\partial x}\Big|_{X_0,Z_0}} + \overline{(z - Z_0)\frac{\partial u_{\mathrm{Lq}}}{\partial z}\Big|_{X_0,Z_0}} + \cdots, \tag{A24}$$

where

$$(x - X_0) = -a\frac{\sigma}{\omega}e^{kZ_0}\sin(kX_0 - \omega t), \tag{A25}$$

$$(z - Z_0) = a\frac{\sigma}{\omega}e^{kZ_0}\cos(kX_0 - \omega t), \tag{A26}$$

$$\frac{\partial u_{\mathrm{Lq}}}{\partial x}\Big|_{X_0,Z_0} = -ak\sigma e^{k(Z_0+\Delta z)}\sin(kX_0 - \omega t), \quad \text{and} \tag{A27}$$

$$\frac{\partial u_{\mathrm{Lq}}}{\partial z}\Big|_{X_0,Z_0} = ak\sigma e^{k(Z_0+\Delta z)}\cos(kX_0 - \omega t). \tag{A28}$$

Hence,

$$\overline{u}_{\mathrm{Lq}} = a^2 k\frac{\sigma^2}{\omega}e^{2kZ_0}e^{k\Delta z}. \tag{A29}$$

As is the case with Stokes drift, the vertical component of the wave-induced bias is zero.

REFERENCES

Amador, A., G. Pawlak, and S. Jaramillo, 2015: ADCP bias and Stokes drift in AUV-based measurements. *2015 IEEE/OES Eleventh Current, Waves and Turbulence Measurement (CWTM 2015)*, IEEE, 304–308, doi:10.1109/CWTM.2015.7098146.

Brown, C. A., Y. Huot, M. J. Purcell, J. J. Cullen, and M. R. Lewis, 2004: Mapping coastal optical and biogeochemical variability using an autonomous underwater vehicle and a new bio-optical inversion algorithm. *Limnol. Oceanogr. Methods*, **2**, 262–281, doi:10.4319/lom.2004.2.262.

Brown, J., C. Tuggle, J. MacMahan, and A. Reniers, 2011: The use of autonomous vehicles for spatially measuring mean velocity profiles in rivers and estuaries. *Intell. Serv. Rob.*, **4**, 233–244, doi:10.1007/s11370-011-0095-6.

Emery, W., and R. Thomson, 1997: *Data Analysis Methods in Physical Oceanography.* Pergamon, 263 pp.

Fong, D. A., and S. G. Monismith, 2004: Evaluation of the accuracy of a ship-mounted, bottom-tracking ADCP in a near-shore coastal flow. *J. Atmos. Oceanic Technol.*, **21**, 1121–1128, doi:10.1175/1520-0426(2004)021<1121:EOTAOA>2.0.CO;2.

——, and N. L. Jones, 2006: Evaluation of AUV-based ADCP measurements. *Limnol. Oceanogr. Methods*, **4**, 58–67, doi:10.4319/lom.2006.4.58.

González-Castro, J. A., and M. Muste, 2007: Framework for estimating uncertainty of ADCP measurements from a moving boat by standardized uncertainty analysis. *J. Hydraul. Eng.*, **133**, 1390–1410, doi:10.1061/(ASCE)0733-9429(2007)133:12(1390).

Goodman, L., and Z. Wang, 2009: Turbulence observations in the northern bight of Monterey Bay from a small AUV. *J. Mar. Syst.*, **77**, 441–458, doi:10.1016/j.jmarsys.2008.11.004.

——, E. R. Levine, and Z. Wang, 2010: Subsurface observations of surface waves from an autonomous underwater vehicle. *IEEE J. Oceanic Eng.*, **35**, 779–784, doi:10.1109/JOE.2010.2060551.

Gordon, R. L., 1996: Acoustic Doppler current profiler: Principles of operation; A practical primer. 2nd ed. Teledyne RD Instruments, 52 pp., http://www.comm-tec.com/Library/Technical_Papers/RDI/Broadband%20Primer.pdf.

Hashimoto, N., 1997: Analysis of the directional wave spectrum from field data. *Advances in Coastal and Ocean Engineering*, P. L.-F. Liu, Ed., Vol. 3, World Scientific, 103–144, doi:10.1142/9789812797568_0004.

Haven, S., and E. A. Terray, 2015: Surface wave measurements from an autonomous underwater vehicle. *2015 IEEE/OES Eleventh Current, Waves and Turbulence Measurement (CWTM 2015)*, IEEE, 72–78, doi:10.1109/CWTM.2015.7098106.

Jaramillo, S., and G. Pawlak, 2010: AUV-based observations of rough bed hydrodynamics. *2010 IEEE/OES Autonomous Underwater Vehicles (AUV)*, IEEE, 9 pp., doi:10.1109/AUV.2010.5779649.

Jones, N. L., R. J. Lowe, G. Pawlak, D. A. Fong, and S. G. Monismith, 2008: Plume dispersion on a fringing coral reef system. *Limnol. Oceanogr.*, **53**, 2273–2286, doi:10.4319/lo.2008.53.5_part_2.2273.

Joyce, T. M., 1989: On in situ calibration of shipboard ADCPs. *J. Atmos. Oceanic Technol.*, **6**, 169–172, doi:10.1175/1520-0426(1989)006<0169:OISOSA>2.0.CO;2.

Moline, M. A., and Coauthors, 2005: Remote Environmental Monitoring Units: An autonomous vehicle for characterizing coastal environments. *J. Atmos. Oceanic Technol.*, **22**, 1797–1808, doi:10.1175/JTECH1809.1.

Paull, L., S. Saeedi, M. Seto, and H. Li, 2014: AUV navigation and localization: A review. *IEEE J. Oceanic Eng.*, **39**, 131–149, doi:10.1109/JOE.2013.2278891.

Pawlak, G., and Coauthors, 2009: Development, deployment, and operation of Kilo Nalu nearshore cabled observatory. *OCEANS 2009—Europe*, IEEE, 133–142, doi:10.1109/OCEANSE.2009.5278149.

Rogowski, P., E. Terrill, and J. Chen, 2014: Observations of the frontal region of a buoyant river plume using an autonomous underwater vehicle. *J. Geophys. Res. Oceans*, **119**, 7549–7567, doi:10.1002/2014JC010392.

Sgarioto, D. E., 2011: The influence of shallow water waves on the REMUS autonomous underwater vehicle. Defence Technology Agency Rep. 330, NR 1582, 76 pp.

Stansfield, K., and Coauthors, 2001: Deep-sea, high-resolution, hydrography and current measurements using an autonomous underwater vehicle: The overflow from the Strait of Sicily. *Geophys. Res. Lett.*, **28**, 2645–2648, doi:10.1029/2000GL012770.

——, G. Gasparini, and D. Smeed, 2003: High-resolution observations of the path of the overflow from the Sicily Strait. *Deep-Sea Res. I*, **50**, 1129–1149, doi:10.1016/S0967-0637(03)00099-2.

Sumner, E. J., and Coauthors, 2013: First direct measurements of hydraulic jumps in an active submarine density current. *Geophys. Res. Lett.*, **40**, 5904–5908, doi:10.1002/2013GL057862.